



**AFRL-RZ-WP-TP-2012-0178**

# **ENDWALL LOSS AND MIXING ANALYSIS OF A HIGH LIFT LOW PRESSURE TURBINE CASCADE (PREPRINT)**

**M. Eric Lyall and Paul I. King**

**Air Force Institute of Technology**

**Rolf Sondergaard**

**Turbine Branch**

**Turbine Engine Division**

**MAY 2012**

**Approved for public release; distribution unlimited.**

*See additional restrictions described on inside pages*

**STINFO COPY**

**AIR FORCE RESEARCH LABORATORY  
PROPULSION DIRECTORATE  
WRIGHT-PATTERSON AIR FORCE BASE, OH 45433-7251  
AIR FORCE MATERIEL COMMAND  
UNITED STATES AIR FORCE**

REPORT DOCUMENTATION PAGE				Form Approved OMB No. 0704-0188	
<p>The public reporting burden for this collection of information is estimated to average 1 hour per response, including the time for reviewing instructions, searching existing data sources, gathering and maintaining the data needed, and completing and reviewing the collection of information. Send comments regarding this burden estimate or any other aspect of this collection of information, including suggestions for reducing this burden, to Department of Defense, Washington Headquarters Services, Directorate for Information Operations and Reports (0704-0188), 1215 Jefferson Davis Highway, Suite 1204, Arlington, VA 22202-4302. Respondents should be aware that notwithstanding any other provision of law, no person shall be subject to any penalty for failing to comply with a collection of information if it does not display a currently valid OMB control number. <b>PLEASE DO NOT RETURN YOUR FORM TO THE ABOVE ADDRESS.</b></p>					
1. REPORT DATE (DD-MM-YY) May 2012		2. REPORT TYPE Conference Paper Preprint		3. DATES COVERED (From - To) 01 January 2011 – 01 January 2012	
4. TITLE AND SUBTITLE ENDWALL LOSS AND MIXING ANALYSIS OF A HIGH LIFT LOW PRESSURE TURBINE CASCADE (PREPRINT)				5a. CONTRACT NUMBER In-house	
				5b. GRANT NUMBER	
				5c. PROGRAM ELEMENT NUMBER 61102F	
6. AUTHOR(S) M. Eric Lyall and Paul I. King (AFIT) Rolf Sondergaard (AFRL/RZTT)				5d. PROJECT NUMBER 2307	
				5e. TASK NUMBER NP	
				5f. WORK UNIT NUMBER 2307NP02	
7. PERFORMING ORGANIZATION NAME(S) AND ADDRESS(ES) Air Force Institute of Technology (AFIT) Wright-Patterson AFB, OH 45433				8. PERFORMING ORGANIZATION REPORT NUMBER AFRL-RZ-WP-TP-2012-0178	
9. SPONSORING/MONITORING AGENCY NAME(S) AND ADDRESS(ES) Air Force Research Laboratory Propulsion Directorate Wright-Patterson Air Force Base, OH 45433-7251 Air Force Materiel Command United States Air Force				10. SPONSORING/MONITORING AGENCY ACRONYM(S) AFRL/RZTT	
				11. SPONSORING/MONITORING AGENCY REPORT NUMBER(S) AFRL-RZ-WP-TP-2012-0178	
12. DISTRIBUTION/AVAILABILITY STATEMENT Approved for public release; distribution unlimited.					
13. SUPPLEMENTARY NOTES Conference paper submitted to the Proceedings of ASME Turbo Expo 2012, to be held in Copenhagen, Denmark on June 11-15, 2012. PA Case Number: 88ABW-2012-2502; Clearance Date: 26 Apr 2012. Report contains color.					
14. ABSTRACT A high lift LPT profile designated L2A is used as a test bed for studying the origin of endwall mixing loss and the role of vortical structures in loss development. It is shown analytically and experimentally that the mixing forces within the endwall wake can be decoupled into either mean flow or turbulent forces, and can be further classified as either reversible or irreversible. Among the irreversible forces, mean flow shear is negligible compared to turbulent shear, suggesting that turbulence dissipation is the dominant cause of loss generation. As a result, the mean flow components of the vortical structures do not generate significant mixing losses. Rather than mixing effects, the mean flow of the vortices cause the suction surface boundary layer to separate inside the passage, thereby generating the large low energy regions typical of endwall flows. Losses are generated as the low energy regions mix out. This vortex separation effect is demonstrated with an experiment using a profile fence and pressure surface modification near the endwall.					
15. SUBJECT TERMS Low pressure turbine, turbine aerodynamics, end-wall loss					
16. SECURITY CLASSIFICATION OF:			17. LIMITATION OF ABSTRACT: SAR	18. NUMBER OF PAGES 18	19a. NAME OF RESPONSIBLE PERSON (Monitor) Rolf Sondergaard 19b. TELEPHONE NUMBER (Include Area Code) N/A
a. REPORT Unclassified	b. ABSTRACT Unclassified	c. THIS PAGE Unclassified			

GT2012-68709

## ENDWALL LOSS AND MIXING ANALYSIS OF A HIGH LIFT LOW PRESSURE TURBINE CASCADE

**M. Eric Lyall**

Air Force Institute of Technology  
Wright-Patterson AFB, OH, USA

**Paul I. King**

Air Force Institute of Technology  
Wright-Patterson AFB, OH, USA

**Rolf Sondergaard**

Air Force Research Laboratory  
Wright-Patterson AFB, OH, USA

### ABSTRACT

A high lift LPT profile designated L2A is used as a test bed for studying the origin of endwall mixing loss and the role of vortical structures in loss development. It is shown analytically and experimentally that the mixing forces within the endwall wake can be decoupled into either mean flow or turbulent forces, and can be further classified as either reversible or irreversible. Among the irreversible forces, mean flow shear is negligible compared to turbulent shear, suggesting that turbulence dissipation is the dominant cause of loss generation. As a result, the mean flow components of the vortical structures do not generate significant mixing losses. Rather than mixing effects, the mean flow of the vortices cause the suction surface boundary layer to separate inside the passage, thereby generating the large low energy regions typical of endwall flows. Losses are generated as the low energy regions mix out. This vortex separation effect is demonstrated with an experiment using a profile fence and pressure surface modification near the endwall. The findings in this paper suggest that profile modifications near the endwall that suppress suction surface separation may provide loss reductions additive to those that weaken vortical structures, such as endwall contouring.

### NOMENCLATURE

$a_{ij}$  turbulence anisotropy tensor,  $\langle u_i u_j \rangle - \frac{2}{3} k \delta_{ij}$   
 $C_{ax}$  axial chord  
 $C_p$  pressure coefficient,  $C_p = (P_s - P_{s,in}) / 0.5 \rho U_{in,st}^2$   
 $C\omega_s$  secondary vorticity coefficient, Eq. (15)  
 $e$  internal energy

$F_{<uv>'}$  secondary mixing force due to  $<uv>'$ , Eq. (17)  
 $F_{<uw>'}$  secondary mixing force due to  $<uw>'$ , Eq. (18)  
 $F_{M'}$  secondary mixing force due to mean flow friction, Eq. (16)  
 $h$  enthalpy  
 $H$  airfoil height, or span  
 $IMF$  irreversible mean force, Eq. (11)  
 $ITF$  irreversible turbulent force, Eq. (13)  
 $k$  turbulent kinetic energy,  $k = 0.5(<u^2> + <v^2> + <w^2>)$   
 $M$  Mach number  
 $MW_{st}$  mechanical work along streamline, Eq. (14)  
 $L$  turbulence integral scale  
 $\bar{n}$  unit vector in mean flow direction  
 $P_s$  static pressure  
 $P_t$  total pressure  
 $RANS$  Reynolds-averaged Navier-Stokes  
 $Re$  Reynolds number based on inlet velocity and axial chord  
 $Re_0$  inlet boundary layer momentum thickness Reynolds number  
 $RMF$  reversible mean force, (See Table 1)  
 $RTF$  reversible turbulent force, Eq. (12)  
 $S$  cascade pitchwise spacing

$S_{ij}$  instantaneous strain rate tensor,  $0.5 \left( \frac{\partial v_j}{\partial x_i} + \frac{\partial v_i}{\partial x_j} \right)$

$s_{ij}$  fluctuation strain rate tensor,  $0.5 \left( \frac{\partial u_j}{\partial x_i} + \frac{\partial u_i}{\partial x_j} \right)$

$SKE$  secondary kinetic energy,  $0.5(V'^2 + W^2)$

$t$  time variable

1

This material is declared a work of the U.S. Government and is not subject to copyright protection in the United States.

Approved for public release; distribution unlimited

Disclaimer: The views expressed in this presentation are those of the authors and do not reflect the official policy or position of the United States Air Force, Department of Defense, or the U.S. Government.

TKE	same as $k$ , used in text for convenience
Tu	turbulence intensity, $\sqrt{\langle u^2 \rangle}/U \times 100\%$
$u_i$	fluctuation velocity vector, $v_i - U_i$
$U_i$	mean velocity vector, $v_i - u_i$
$v_i$	instantaneous velocity vector
$U, V, W$	cascade mean velocities
$U', V', W$	secondary mean velocities
$x_i$	Cartesian index notation direction coordinate
$x, y, z$	cascade coordinate directions
$x', y', z$	secondary coordinate directions
$Y$	total pressure loss coefficient,
	$Y = \left( P_t - P_{t, in} \right) / 0.5 \rho U_{in, st}^2$
$Z_w$	Zweifel loading coefficient,
	$Z_w = 2 \left( \frac{S}{C_{ax}} \right) \cos^2 \alpha_{ex} (\tan \alpha_{in} - \tan \alpha_{ex})$

### Greek

$\alpha$	cascade gas angle, measured from axial
$\delta_{ij}$	Kronecker delta
$\delta_{99}$	99% inlet boundary layer thickness
$\epsilon_{ijk}$	alternating unit tensor
$\rho$	fluid density
$\nu$	fluid kinematic viscosity
$\omega_i$	mean vorticity vector, $\epsilon_{ijk} \partial_j U_k$

### Subscripts and Superscripts

ex	exit location
$i, j, k$	Cartesian indices, can be 1, 2, or 3
in	inlet location
st	streamwise direction
$x, y, z$	direction indicators for axial, pitchwise, and spanwise directions, respectively
( )'	prime indicates secondary coordinate system

### Operator Symbols

$\nabla$	gradient operator of scalar field
$\Delta$	difference operator
$\langle \rangle$	averaging operator

## INTRODUCTION

Recently, there has been increased interest in increasing the aerodynamic load on turbine airfoils to reduce weight. Turbines operate with an overall favorable pressure gradient, but with diffusion on the airfoil suction surfaces, increasing the aerodynamic load with highly curved airfoils and stronger adverse pressure gradients can cause stall at higher Reynolds numbers. Stall refers to a separation bubble that does not reattach upstream of the trailing edge. McQuilling [1] showed that with laminar-turbulent transition modeling and manipulation of the pressure loading distribution, high lift profiles can be designed that preserve midspan low Reynolds number performance. In linear cascade studies using profiles

with similar gas angles as the L2A in the present study, Praisner et al. [2] and Knezevici et al. [3] showed that such designs increase endwall loss beyond practical limits. In both of these studies, the authors applied non-axisymmetric endwall contouring in an attempt to mitigate the elevated endwall losses, yet the losses remained too high for use in engines.

The purpose of this paper is to elucidate the causes of elevated endwall loss for high lift LPT airfoil designs and to suggest an alternative approach for reducing mixing losses. Past endwall loss reduction methods such as endwall contouring have generally focused on weakening vortical structures. Vortices are often viewed in the literature as loss-generating mechanisms, yet the way they contribute to loss is unclear.

In this paper we examine endwall flow and losses in terms of both mixing effects and the interaction of vortices with the profile suction surface. Past endwall loss studies have considered mixing effects, but interaction of the endwall flow with the profile has not received much attention. To study mixing we decompose the mixing forces locally within the flow field. The interaction of vortices with the profile is studied using profile boundary layer fences and a pressure surface modification. Because of the no-slip condition, little can be done to reduce endwall boundary layer losses for a given surface area, so the focus of this work is on aspects of freestream mixing.

## ENDWALL LOSS STUDIES

The mean endwall flow field is comprised of several vortical structures with the passage vortex being dominant. Although large scale unsteady flow features may be present, turbulence is also quite high in the endwall region. As a result, past endwall loss studies have generally focused on dissipation of the vortical structures by studying the secondary kinetic energy (SKE) and the role of turbulence.

### The Role of Secondary Kinetic Energy

In the mean flow field, the rotational energy at the endwall is typically quantified by the magnitude of SKE. Using the mass-averaged exit flow angle, or the mean camber line angle at the trailing edge as the primary reference direction (depends on researcher), SKE is defined as half the sum of squared mean velocity components normal to the primary reference direction (See Fig. 2). The mathematical definition is given as,

$$SKE = \frac{1}{2} (\mathbf{v}'^2 + \mathbf{W}^2) . \quad (1)$$

Moore and Adhye [4] measured SKE at three downstream planes of a low speed linear turbine cascade. They suggested that the increased loss is almost entirely explained by a decrease in SKE at downstream planes. More recently, MacIsaac et al. [5] also reported endwall flow loss development downstream of a low speed linear turbine cascade. They observed that reduction in SKE only accounted for 42% and 64% of the mixing losses in the second and third downstream mixing planes, respectively. The lack of correlation between

SKE and loss was attributed to streamwise gradients in the exit flow that were not captured by computing SKE.

The differing conclusions of these two studies regarding SKE may be due to boundary conditions. It is worth noting that the Moore and Adhye [4] cascade had an aspect ratio of unity, whereas the MacIsaac et al. [5] cascade had an aspect ratio of 2.8. Besides incompressible flow, no other geometric or flow conditions were matched. The significant differences in test conditions provide a good pair of test cases for assessing the utility of SKE as an indicator of passage loss. The differing conclusions suggest that SKE may not be a good indicator of measured losses. We do not present SKE measurements in the present study.

### **The Role of Turbulence**

Gregory-Smith et al. [6] investigated the role of TKE in total pressure loss within and downstream of a low speed linear cascade of turbine airfoils. The through-passage integrated turbulence energy increased tenfold, but it only accounted for about 25% of the total pressure loss. They concluded that dissipation (presumably mean flow and turbulent) through viscous action is very significant. MacIsaac et al. [5], however, found that the integrated TKE in three measurement planes downstream of their linear turbine cascade remained approximately constant, indicating that the growth of TKE is not correlated with increasing downstream total pressure loss.

Moore et al. [7] studied turbulent Reynolds stresses in downstream mixing in a low speed linear turbine cascade. They found that the integrated deformation work term that exchanges mean flow and turbulent kinetic energy (TKE) (also called the turbulence production term) agreed very closely with the rate of total pressure loss production. Their data also showed that contours of TKE identified the boundary of the airfoil wake similar to loss coefficient contours, but the peaks were not aligned. MacIsaac et al. [5] also studied the turbulence production in downstream measurement planes of a low speed linear turbine cascade. Their results supported Moore et al. [7], in that turbulence production (not simply TKE) plays a significant role in the mixing process and loss production. MacIsaac et al. [5] pointed out that the magnitude of the turbulence production term should be comparable to the dissipation term.

### **Relation of Present Work to Past Mixing Loss Studies**

The mixing analysis in this paper is related to the work of MacIsaac et al. [5] and Moore et al. [7], but the governing equation we use is quite different. These authors applied the mean kinetic energy equation for a turbulent flow given by Hinze [8]. That equation has a gradient of the product of a convection velocity and total pressure, a term that is difficult to measure. Moore et al. [7] assumed the convection velocity constant so it could be factored out for computing area averages of the total pressure gradient downstream of the blade row. In this paper we solve for the total pressure gradient to study mixing locally in the flow field.

### **MIXING ANALYSIS**

For incompressible and adiabatic cascade flows the overall work is zero. For these conditions the first law of thermodynamics can be written as,

$$\frac{\Delta P_t}{\rho} = -\Delta e, \quad (2)$$

where  $e$  is internal energy. We see that the passage total pressure loss will be due to an increase in internal energy. Considering a differential element in the flow field, the equation governing the internal energy of an incompressible, adiabatic, turbulent flow can be written as,

$$\frac{D\langle e \rangle}{Dt} = 2\nu \left[ \langle S_{ij} \rangle \langle S_{ij} \rangle + \langle s_{ij} s_{ij} \rangle \right], \quad (3)$$

where  $\langle e \rangle$  is the mean internal energy,  $\langle S_{ij} \rangle$  is the mean strain rate tensor, and  $s_{ij}$  is the fluctuation strain rate tensor. The quantities  $2\nu \langle S_{ij} \rangle \langle S_{ij} \rangle$  and  $2\nu \langle s_{ij} s_{ij} \rangle$  are the mean flow and turbulence dissipation rates, respectively. These dissipation terms are caused by shear stresses in the fluid. To decouple the roles of the mean and turbulent flow fields in loss production, one could locally measure both dissipation rates to obtain a direct measure of internal energy production and total pressure loss. Integrating the local dissipation measurements across the passage would yield the overall total pressure loss production rate. Unfortunately, measurement of the turbulence dissipation rate is very difficult even for simple flows due to the need to measure instantaneous fluctuation gradients.

An alternative method to quantify local influences on total pressure can be derived from the RANS momentum equation,

$$\frac{\partial U_i}{\partial t} + U_j \frac{\partial U_i}{\partial x_j} = -\frac{1}{\rho} \frac{\partial P_s}{\partial x_i} + \nu \frac{\partial^2 U_i}{\partial x_j \partial x_j} - \frac{\partial \langle u_i u_j \rangle}{\partial x_j}. \quad (4)$$

The convection term on the left hand side can be replaced using the following identity given by Panton [9],

$$U_j \frac{\partial U_i}{\partial x_j} = \frac{\partial}{\partial x_i} \left( \frac{1}{2} U_j U_j \right) + \varepsilon_{ijk} \omega_j U_k, \quad (5)$$

where  $\omega_j$  is the local vorticity vector. Note that the second term on the right hand side of Eq. (5) can also be written as  $\vec{\omega} \times \vec{U}$ . Assuming steady mean flow and substituting Eq. (5) into Eq. (4), we obtain an expression for the spatial total pressure derivatives,

$$\frac{\partial P_t}{\partial x_i} = \mu \frac{\partial^2 U_i}{\partial x_j \partial x_j} - \rho \varepsilon_{ijk} \omega_j U_k - \rho \frac{\partial \langle u_i u_j \rangle}{\partial x_j}. \quad (6)$$

Equation (6) can be interpreted as a local description of the force balance in the flow field that causes changes in total pressure. The first term on the right hand side represents a force due to viscous diffusion, an irreversible mean flow friction force (IMF). The second term came from the vector identity of Eq. (5) and represents a coriolis force. This vector identity decomposed the convection term present in the inviscid Euler equations and as a result, is a reversible mean force (RMF). The last term of Eq. (6) requires more attention.

Following Pope [10], the Reynolds stress tensor can be decomposed as,

$$\langle u_i u_j \rangle = \frac{2}{3} k \delta_{ij} + a_{ij} \quad (7)$$

where  $k = 0.5 \langle u_i u_i \rangle$ . This decomposition splits the Reynolds stress tensor into isotropic and anisotropic parts,  $\frac{2}{3} k \delta_{ij}$  and  $a_{ij}$ , respectively. The isotropic stress cannot cause shear and as a result, represents a reversible turbulent force (RTF). This is analogous to the absence of pressure from the vorticity equation because of its inability to cause shear. On the other hand,  $a_{ij}$  represents a deviatoric shear stress and as a result, accounts for an irreversible turbulent force (ITF). In summary, we have irreversible mean forces (IMF), irreversible turbulent forces (ITF), reversible mean forces (RMF), and reversible turbulent forces (RTF) that define the total pressure spatial derivatives.

For experiments, it is convenient to non-dimensionalize equations for establishing similarity and to enable scaling. In this study, spatial variables were scaled using the axial chord. Total pressure was scaled by twice the inlet dynamic head. Velocities were scaled by the inlet mean velocity magnitude and turbulence quantities by the square of the inlet mean velocity magnitude. In non-dimensional variables, Eq. (6) can be expressed as,

$$\frac{\partial P_t}{\partial x_i} = \frac{1}{\text{Re}} \frac{\partial^2 U_i}{\partial x_j \partial x_j} - \varepsilon_{ijk} \omega_j U_k - \left( \frac{2}{3} \frac{\partial k}{\partial x_j} \delta_{ij} + \frac{\partial a_{ij}}{\partial x_j} \right). \quad (8)$$

For convenience, the index notation terms of Eq. (8) are written out explicitly in Table 1 with non-dimensional variables for the x-direction. The forms of the total pressure derivatives in the y and z directions are implied. To expand the index notation terms, substituting 1, 2, or 3 for the indices (i.e., i, j, and k) refers to the x, y, and z coordinate directions, respectively. Table 2 lists the scales used for non-dimensionalization.

Because Eq. (8) is an alternative form of the RANS momentum equation (a vector equation), taking the dot product of Eq. (8) with the mean velocity vector will result in a mechanical energy equation. The forces will generate work in the flow. By taking the dot product of Eq. (8) with a unit vector in the mean flow direction, we obtain a measure of the change in total pressure along the local streamline, referred to as the mechanical work,

$$MW_{st} = \nabla P_t \cdot \bar{n}, \quad (9)$$

where,

$$\nabla P_t = \frac{\partial P_t}{\partial x} \bar{i} + \frac{\partial P_t}{\partial y} \bar{j} + \frac{\partial P_t}{\partial z} \bar{k}, \quad (10)$$

and  $\bar{n}$  is the unit vector in the mean flow direction.  $MW_{st}$  is our focus for determining the dominant mixing effects. Upon carrying out the calculation of  $MW_{st}$  by hand, one finds that the second term on the right hand side of Eq. (8) (i.e., term defining RMF) is orthogonal to the mean velocity vector. Thus, RMF has no role in changing the mechanical energy of the flow. The remaining mixing effects are decoupled according to,

$$IMF = IMF_x n_x + IMF_y n_y + IMF_z n_z, \quad (11)$$

**Table 1.** Expansion of Eq. (8) for the x-direction

$\frac{\partial P_t}{\partial x} = IMF_x + RMF_x + RTF_x + ITF_x$	
$IMF_x$	$\frac{1}{\text{Re}} \left( \frac{\partial^2 U}{\partial x^2} + \frac{\partial^2 U}{\partial y^2} + \frac{\partial^2 U}{\partial z^2} \right)$
$RMF_x$	$(-1)(\omega_y W - \omega_z V)$
$RTF_x$	$\left( -\frac{2}{3} \right) \frac{\partial k}{\partial x}$
$ITF_x$	$(-1) \left( \frac{\partial a_{uu}}{\partial x} + \frac{\partial a_{uv}}{\partial y} + \frac{\partial a_{uw}}{\partial z} \right)$

**Table 2.** Summary of Scaling Variables

Quantity	Scale
$P_t$	$\rho U_{in,st}^2$
Velocity	$U_{in,st}$
Flucuation/Re Stress	$U_{in,st}^2$
Distance	$C_{ax}$

$$RTF = RTF_x n_x + RTF_y n_y + RTF_z n_z, \quad (12)$$

$$ITF = ITF_x n_x + ITF_y n_y + ITF_z n_z, \quad (13)$$

and,

$$MW_{st} = IMF + RTF + ITF. \quad (14)$$

## EXPERIMENTAL METHODS

The experiments were conducted in the AFRL low speed wind tunnel facility located at Wright-Patterson Air Force Base. This wind tunnel is an open loop induction type, with the flow that enters a bell-mouth contraction passing through a turbulence-generating grid, through a cascade and exiting via a fan. The turbulence grid is comprised of a lattice of horizontal and vertical 25.4 mm round bars, with 76.2 mm center spacing. The turbulence grid produces a turbulence intensity of  $Tu = 2.9\%$ , with an integral scale of  $L_{in} = 19.7$  mm at about  $1.4C_{ax}$  upstream of the cascade, where  $C_{ax}$  is axial chord. The center blade of the cascade is approximately 90 bar diameters downstream of the grid.

A schematic of the test section is given in Fig. 1. The cascade is comprised of seven airfoils. The outer tailboard is used to set the exit angle at  $\text{Re} = 100,000$ , the Reynolds number used in this study. A splitter plate assembly provides inlet boundary layer control for endwall studies. The distance between the splitter plate and the tunnel roof causes an effective span to axial chord ratio of 3.5. The splitter inlet plate leading edge was designed according to the recommendations of Narasimha and Prasad [11].

Figure 2 shows the cascade and secondary flow coordinate systems. The secondary coordinate system is indicated with primes and rotated  $58^\circ$  off axial, the approximate exit angle for tests with and without fences. Exit measurements were taken  $0.58C_{ax}$  downstream of the blade row, placing the center airfoil

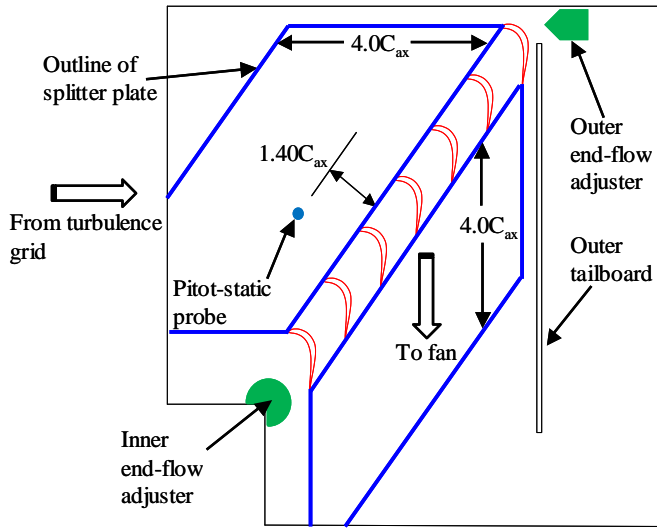


**Figure 1.** Schematic of AFRL low speed wind tunnel test section

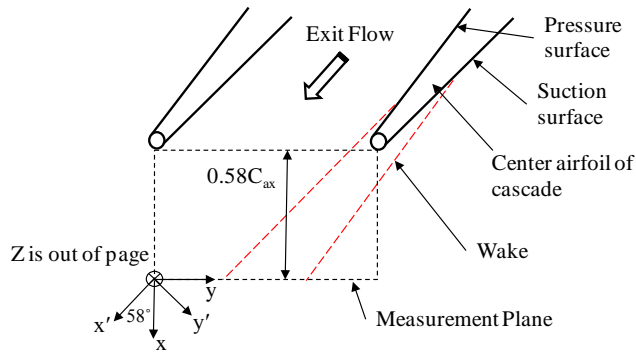


**Figure 2.** Schematic depicting the cascade and secondary flow (primed) coordinate system definitions

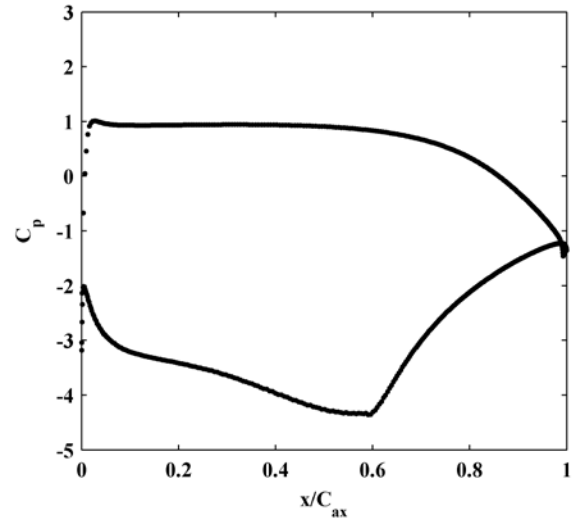
wake near the middle of the measurement plane. Table 3 summarizes the cascade geometry and flow conditions. One notes in Table 3 that the inlet boundary layer thickness is quite small. Though the inlet boundary layer thickness will influence the overall measured losses downstream of the blade row, this paper focuses on the physics of how losses are generated and not on the overall losses.

Figure 3 shows the pressure loading of the L2A profile. The pressure loading is based on fully turbulent calculations by Lyall et al. [12], and shows that the profile is aft loaded with peak suction at  $0.60C_{ax}$ . This profile was designed at the Propulsion Directorate of the Air Force Research Laboratory for studying low Reynolds number and high lift aerodynamics. It was designed to have the same gas angles as the Pratt & Whitney Pack B profile.

Except for ambient pressures, data were sampled using National Instruments hardware and software. An upstream stationary pitot-static probe and a kiel probe in the exit measurement plane were used to measure total pressure loss. At 3.2 mm diameter, the kiel probe was less than 2% of the

**Table 3.** Cascade Geometry and Flow Conditions

Axial chord, $C_{ax}$	152.4 mm
Pitch/axial chord, $S/C_{ax}$	1.221
Span/axial chord, $H/C_{ax}$	3.5
Zweifel coefficient, $Z_w$	1.59
Inlet flow angle (from axial), $\alpha_{in}$	$35^\circ$
Mean exit flow angle without fence (from axial), $\alpha_{ex}$	$-57.7^\circ$
Inlet turbulence Intensity, $Tu_{in}$	2.9%
Streamwise integral scale at inlet, $L_{in,st}$	$0.13C_{ax}$
Max exit Mach number, $M_{ex}$	0.053
$Re$ , ( $U_{in,st}$ and $C_{ax}$ )	100,000
Inlet boundary layer parameters, $1.4C_{ax}$ upstream	
$\delta_{99}/H$	0.025
$Re_\theta$	655
Shape factor	2.2



**Figure 3.** Pressure loading of the L2A profile, taken from Lyall et al. [12]

blade pitch, providing sufficient resolution within the wakes. The ambient pressure was measured with a laboratory barometer, and freestream fluid temperatures were measured using type J thermocouples. An IFA300 constant temperature anemometer was used with single normal hot-film probes (TSI 1211-20) for obtaining velocities and turbulence measurements at the inlet. The velocities for setting the inlet Reynolds number were measured using the upstream pitot-static probe. A TSI 1299-20-18 triple sensor hot-film probe was used to obtain velocity and turbulence measurements downstream of the blade row. The three sensors of the triple probe were contained within a 2 mm measurement diameter. The probe stem was 4.6 mm in diameter.

All hot-film probes were calibrated using a TSI Model 1127 velocity calibrator. Typical calibration curves included 18

points, spanning the measured velocity range in the experiment. Calibrations spanned  $2 < U < 14$  m/s and  $5 < U < 29$  m/s for inlet and exit measurements, respectively. During calibration, the triple sensor probe was placed in a zero pitch/yaw configuration for the entire velocity range. An analytical technique, similar to that described by Lekakis et al. [13], combined with the table look-up procedure of Gieseke and Guezennec [14] was used for obtaining velocity magnitudes and angles, given effective cooling velocities. In the experiment, average flow angles relative to the probe axis were typically within  $10^\circ$ . Angle measurements on the calibration stand were within  $\pm 0.9^\circ$  of the actual velocity vector for  $\pm 18^\circ$  pitch and yaw, indicating reasonable bias error.

All uncertainties were estimated at 95% confidence. Uncertainties for the Reynolds number and total pressure loss coefficients were estimated using the partial derivative and root-sum-square method of Kline and McClintock [15]. The loss coefficients at each point were estimated to within  $\pm 0.01$ , approximately 1% of the inlet dynamic head. The Reynolds number was also estimated to be within about 1% of the measured value. The uncertainty of mean velocities for the exit flow field was estimated to be within 1.5% of the measured values. Sampling times were also sufficiently long to ensure independence of the samples in the presence of unsteadiness. When acquiring data for computing three-dimensional mixing forces, it was important to control the precision error to allow quality gradient calculations within the turbulence field. Approximately 7,000 independent samples were acquired at each measurement location to limit the mean-square fluctuation to within 3.5% of the measured values.

Three-dimensional mixing forces were obtained from triple sensor hot-film measurements. Derivatives were calculated using second order centered finite differences given by Tannehill et al. [16] for three-point stencils without interpolation between measurement points. For computing the derivatives, the grid spacing was set at  $\Delta x = 0.083C_{ax}$ ,  $\Delta y = 0.028C_{ax}$ , and  $\Delta z = 0.042C_{ax}$  within the measurement plane. Forty five independent quantities comprised of velocity and turbulence measurements were required to compute the mechanical work,  $MW_{st}$ , at a single position. The combined uncertainty in  $MW_{st}$  due to the separate measurements was estimated using the sequential perturbation technique of Moffat [17].

Results of  $MW_{st}$  with 95% confidence bands at 20% span, along with total pressure loss coefficients for reference are shown in Fig. 4. Positive and negative  $MW_{st}$  indicates energy addition to and extraction from the mean flow, respectively. As will be shown in the results section, the differences in the mixing forces that sum together to give  $MW_{st}$  are larger than the error bars, indicating that meaningful conclusions can be obtained regarding the role of the different mixing forces. The Reynolds stress measurements had the largest uncertainty.

## RESULTS AND DISCUSSION

The experimental results are presented in three subsections. The first includes a discussion of the flow field to provide a

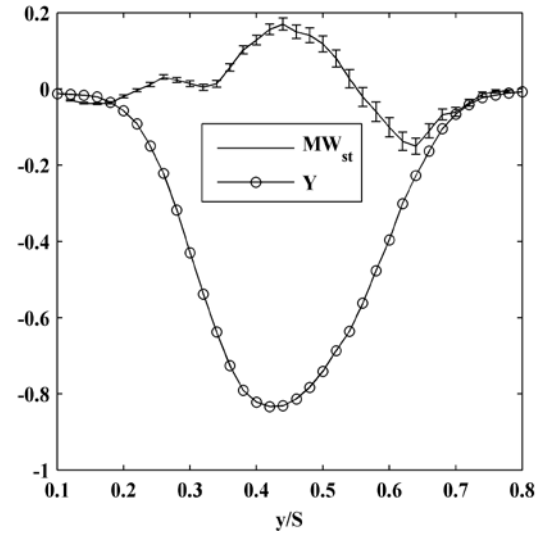


**Figure 4.** Mechanical work and loss coefficients at 20% span in the measurement plane (See Fig. 2)

basis for discussing mixing and loss development. Mixing forces are discussed next, whereby the mean flow and turbulence effects are decoupled. The final subsection presents an experiment in the lab using profile fences and a pressure surface modification. The purpose of this latter experiment was to investigate the influence on loss development due to interaction of the secondary flow with the profile suction surface.

## Flow Field Description

Secondary flow formation is well documented so only a brief discussion will be given here, based on Langston's [18] review. Several variations of endwall flow models exist, but we will only consider the dominant features. Upstream of the leading edge, the inlet endwall boundary layer separates, forming a horseshoe vortex. The pressure side leg of the horseshoe vortex is swept across the passage towards the adjacent suction surface by the cross passage pressure gradient, eventually becoming the passage vortex. The passage vortex climbs the suction surface and separates as it rotates. Meanwhile, the suction side leg of the horseshoe vortex remains close to the suction surface and rotates in opposite sense to the passage vortex. Langston [18] also points out that the suction side leg may orbit around the axis of the passage vortex. In this paper, we will focus on mixing effects of the secondary flow structures downstream of the blade row, and also the interaction with the suction surface.

Figure 5 gives surveys of secondary velocity vectors ( $V'$ ,  $W$ ), secondary vorticity coefficients and total pressure loss coefficients. The wake behind the center blade of the cascade is shown where the right side of the wake corresponds to the suction surface (see Fig. 2). The secondary vorticity coefficients were computed using the method described by Hodson and Dominy [19],



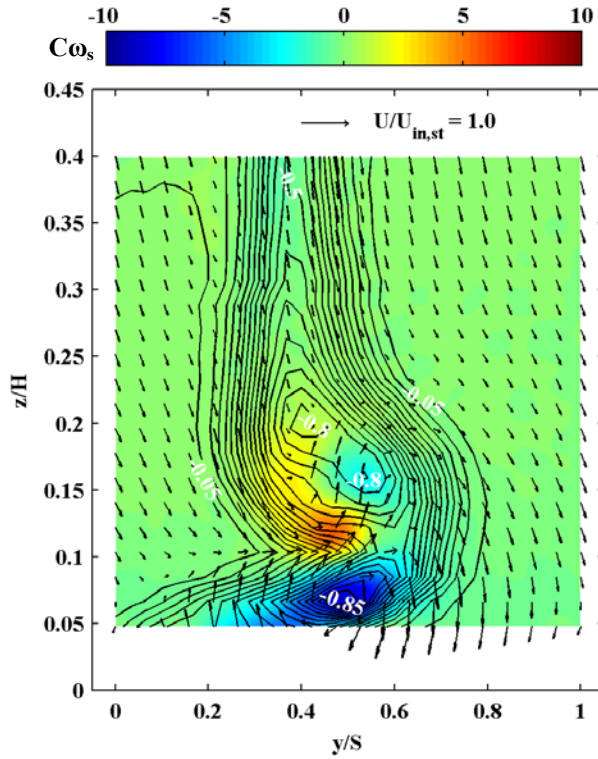


**Figure 5.** Secondary vorticity, total pressure loss coefficients ( $\Delta Y = 0.05$  for contours), and secondary velocity vectors within the measurement plane (See Fig. 2)

$$C\omega_s = \frac{\partial W}{\partial y} - \frac{\partial V'}{\partial z}, \quad (15)$$

where the variables were non-dimensionalized with the scales of Table 2. The positive axis of vorticity is out of the page. Equation (15) will not equal the magnitude of the vorticity vector in the streamwise direction,  $x'$ , but provides a measure of the relative strength of the streamwise vorticity across the measurement area. Also note that there is a  $z$  component of the secondary velocity vectors approaching midspan, a region in the measurement area where the  $z$  component may be expected to be nearly zero. This  $z$  component is due to the extra blockage of the wind tunnel boundary layer at  $z/H = 1.0$ , compared to the relatively thin boundary layer on the tunnel splitter plate at  $z/H = 0$  (See Fig. 1). In this wind tunnel using the splitter plate, the  $z$  component of velocity approaching midspan is smaller for cascades that have less secondary loss.

The center of the passage vortex in Fig. 5 is approximately at  $y/S = 0.48$  and  $z/H = 0.07$ , as indicated by the secondary velocity vectors. The passage vortex extends approximately to  $z/H = 0.10$ . Strong negative vorticity is present inside the passage vortex. The secondary velocity vectors midwake beyond the passage vortex show a spanwise migration of flow towards midspan. Those vectors indicate that this migrating flow extends to approximately  $z/H = 0.20$ . The boundary layer on the suction surface will be skewed due to this migrating flow. Furthermore, the spanwise migration of flow turns away from the suction surface and separates, generating a weaker

negative vorticity core at  $y/S = 0.55$  and  $z/H = 0.16$ . Rather than separate negative vorticity cores, it is more common for the spanwise migrating flow and the passage vortex to be merged, generating a single negative vorticity core within the secondary flow. Zoric et al. [20], however, show data for cascades with the same gas angles as L2A with both merged and separate negative vorticity cores. For incoming turbulence levels of  $Tu = 1.5\%$ , Zoric et al. [20] show that the Pack B cascade generates a single merged region of negative vorticity while the Pack D-A cascade has two negative vorticity cores, similar to L2A in this study. Also note in Fig. 5 that there is a region of positive vorticity that has a peak magnitude at  $y/S = 0.45$  and  $z/H = 0.12$  and extends to nearly  $z/H = 0.20$ . This region of positive vorticity (commonly referred to as the shed vorticity) is due to the skewing of the profile boundary layer by the spanwise flow migration.

The total pressure loss coefficients of Fig. 5 show that there are two regions of low energy cores in the flow field, which is typical of endwall flows. The low energy core closest to the endwall is approximately collocated with the passage vortex, at  $y/S = 0.48$  and  $z/H = 0.07$ . A larger low energy region is approximately centered at  $y/S = 0.45$  and  $z/H = 0.18$  and contains two minima.

In the following sections of this paper, we will investigate the components of Eq. (8) that influence  $MW_{st}$  in Eq. (9). We focus on the irreversible effects of mixing. Secondly, we will investigate how the low energy regions form, but focus on the largest low energy region centered at  $y/S = 0.45$  and  $z/H = 0.18$ . We suggest that the largest low energy region forms inside the passage as the spanwise flow migrating towards midspan separates from the suction surface. Later this idea is investigated using profile fences and a pressure surface modification.

### Decomposition of Mixing Forces

Figure 6 shows  $MW_{st}$  obtained at 20% span within the large low energy region of Fig. 5. Recall from Eq. (14) that IMF, ITF, and RTF sum together to give  $MW_{st}$ . One first notes that the irreversible mean force due to viscous diffusion, IMF, is negligibly small. Secondly, the dominant mixing effect is the irreversible turbulent shear force, ITF. The reversible turbulent force, RTF, plays a secondary role in mixing at this spanwise location. At the positive peak in  $MW_{st}$  ( $y/S = 0.44$ ), the ratio of mean to turbulent shear forces is  $IMF/ITF = 0.003$ . This negligible mean flow shear suggests that turbulence dissipation is the dominant cause of losses at 20% span. We will investigate the shear effects within the measurement plane of Fig. 2 to show that mean flow shear remains negligible compared to turbulent shear at other spanwise locations.

We define some additional terms for convenience to describe the relative strength of shear effects. Consider mixing in the downstream main flow direction,  $x'$  of Fig. 2. By inspection of Table 1 and applying the secondary coordinate system,  $IMF_{x'}$  will define the mean flow shear force in the main flow direction.  $IMF_{x'}$  results from viscous diffusion, or second

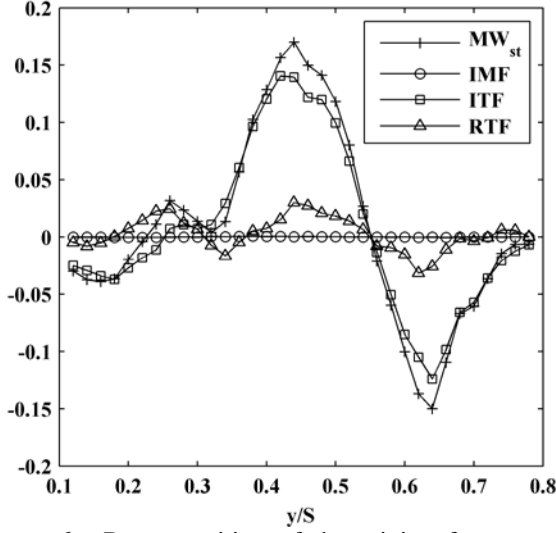


**Figure 6.** Decomposition of the mixing forces at 20% span in the measurement plane (See Fig. 2)

derivatives of the  $U'$  velocity. We define a new mean flow shear force parameter as,

$$F_{M'} = \frac{1}{\text{Re}} \left( \frac{\partial^2 U'}{\partial y^2} + \frac{\partial^2 U'}{\partial z^2} \right), \quad (16)$$

with non-dimensional variables according to Table 2. The diffusion term in the  $x'$  direction was neglected. Also note in Eq. (16) the second derivative in the  $y$  direction as opposed to  $y'$ . This change reflects the measurement plane orientation in the  $y$  direction.  $F_{M'}$  will therefore have a smaller magnitude than expected for  $\text{IMF}_{x'}$ .

Using similar reasoning as for defining  $F_{M'}$ , we define two new turbulent shear force parameters. Recognizing in Eq. (7) that  $\langle u_i u_j \rangle = a_{ij}$  when  $i \neq j$ , these parameters are defined by,

$$F_{\langle uv \rangle'} = - \frac{\partial \langle uv \rangle'}{\partial y}, \quad \text{and} \quad (17)$$

$$F_{\langle uw \rangle'} = - \frac{\partial \langle uw \rangle'}{\partial z}, \quad (18)$$

with non-dimensional variables according to Table 2. The turbulent shear parameters are defined separately to isolate effects due to each Reynolds stress component. The sum of  $F_{\langle uv \rangle'}$  and  $F_{\langle uw \rangle'}$  will have a smaller magnitude than  $\text{ITF}_{x'}$  due to the derivative in the  $y$  direction as opposed to  $y'$ . The implication of Eqs. (16-18) is that if  $F_{M'}/(F_{\langle uv \rangle'} + F_{\langle uw \rangle'})$  is negligible, then  $\text{IMF}_{x'}/\text{ITF}_{x'}$  will also be negligible. For the full area traverse, the velocity and turbulence data were refined using cubic spline interpolation for computing derivatives.

Figure 7 shows flood plots of the newly defined mixing force variables. Contours of  $Y$  and secondary velocity vectors are included for reference. Figure 7a shows the combined effects of  $F_{\langle uv \rangle'}$  and  $F_{\langle uw \rangle'}$ . On the outer perimeter of the wake, the mixing forces are negative, indicating energy extraction from the mean flow. On the inside of the wake, the mixing

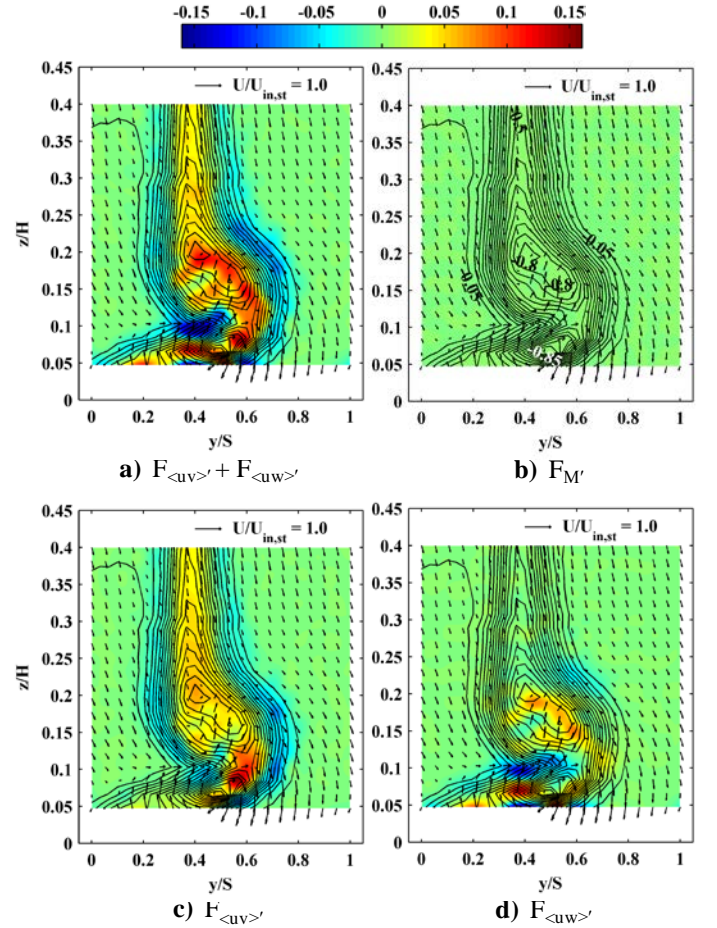


**Figure 7.** Flood plots of mixing force variables overlaid with  $Y$  contours and secondary velocity vectors

forces are positive and adding energy to the mean flow. In Fig. 7b, the mean flow viscous force,  $F_{M'}$ , has a negligible influence across the whole measurement area, thus supporting the original idea that mean flow viscous shear and dissipation has little effect on losses. From Figs. 7c and 7d, we see that  $F_{\langle uv \rangle'}$  remains significant over most of the measurement area.  $F_{\langle uw \rangle'}$ , however, is insignificant from  $z/H = 0.25$  on towards midspan and has little influence on mixing in this region.

Between  $z/H = 0.25$  and the endwall ( $z/H = 0$ ), the region where both  $F_{\langle uv \rangle'}$  and  $F_{\langle uw \rangle'}$  are significant, the mixing forces vary significantly across the measurement area. This variation is enhanced mainly because  $F_{\langle uv \rangle'}$  and  $F_{\langle uw \rangle'}$  do not always carry the same sign. Where both quantities carry the same sign, energy extraction or addition is enhanced to speed up mixing. One such area is  $y/S = 0.4$  and  $z/H = 0.10$  in Fig. 7a. At this location, energy extraction is quite strong. Figures 7c and 7d show that  $F_{\langle uv \rangle'}$  and  $F_{\langle uw \rangle'}$  both extract energy from the mean flow at this location. On the other hand at  $y/S = 0.4$  and  $z/H = 0.15$  in Fig. 7a, the overall mixing force is depressed within the large low energy region. Figures 7c and 7d reveal that  $F_{\langle uv \rangle'}$  and  $F_{\langle uw \rangle'}$  are of opposite sign at this position to slow down mixing.

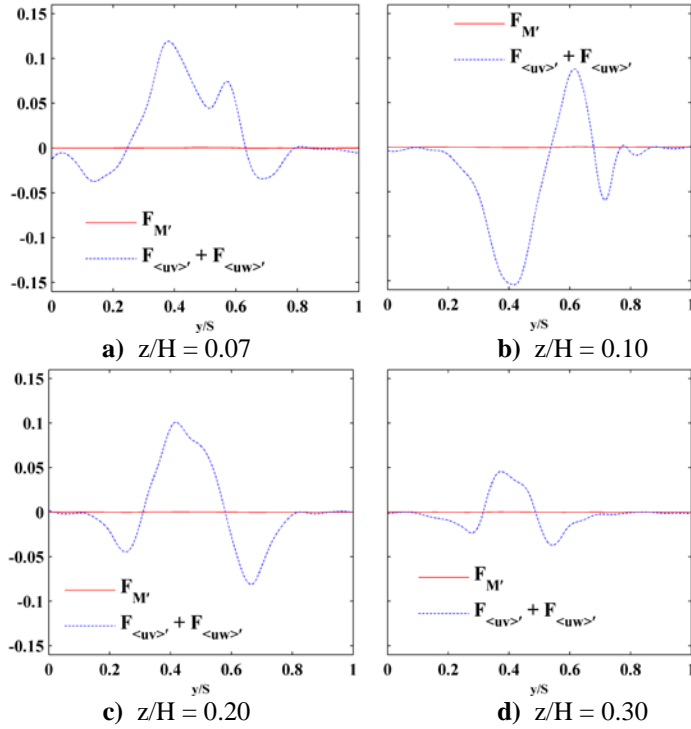


**Figure 8.** Mean flow and viscous effects for various spanwise positions

Figure 8 shows mixing forces obtained from Fig. 7 at several spanwise positions. The  $z/H = 0.07$  position in Fig. 8a corresponds to the approximate center of the passage vortex. At this spanwise location, the turbulent shear forces mostly add energy to the mean flow and  $F_{M'}$  is negligible. Recall from Fig. 5 that the strongest secondary vorticity is within the passage vortex. As an additional check of the magnitude of mean flow shear,  $F_{M'}$  was recalculated at  $z/H = 0.07$  with both  $V'$  and  $W$  as opposed to  $U'$ . The change in  $F_{M'}$  calculated with  $V'$  and  $W$  was negligible, indicating weak mean flow shear effects inside the passage vortex despite the presence of strong secondary vorticity. At  $z/H = 0.10$  in Fig. 8b, energy extraction by the turbulent forces dominates. At  $z/H = 0.20$  and  $0.30$  in Figs. 8c and 8d, respectively, the variation of turbulent mixing forces is geometrically similar across the pitch with smaller magnitudes closer to midspan. At all spanwise locations,  $F_{M'}$  is negligible.

Figures 6 through 8 provide insight into how and where mixing losses are produced in the airfoil wake. Analytically, shear effects in the flow can be decoupled into those that change internal energy and those that change mechanical energy (cf., Panton [9]). Both effects occur simultaneously. The turbulence and mean flow dissipation rates are shear effects that change the internal energy of the flow, leading to the net total pressure loss across the blade row (Eqs. 2 and 3). Because the turbulence dissipation rate is difficult to measure, we used an equation describing the mechanical energy of the flow ( $MW_{st}$  in Eqs. 9 and 14) as a basis for determining the strength of the shear effects in the flow field. The magnitudes of shear effects that change the mechanical energy indicate the

presence and relative strength of dissipation effects. The implication of negligible mean flow shear in Figs. 6 through 8 is that turbulence dissipation is the dominant cause of mixing losses. Furthermore, turbulent shear is strongest in the secondary flow between  $z/H = 0.25$  and the endwall, suggesting higher dissipation rates in this region.

In this section we decomposed the mixing effects of the mean and turbulent flow fields of the airfoil wake. The mean flow component of the vortex structures will have a negligible effect on mixing loss. This conclusion applies to the freestream away from bounding walls. Also, large-scale unsteadiness has been included with the turbulence effects in this analysis. Although mixing losses are negligible for mean flow structures, they do play a role in loss production, primarily in how they interact with the suction surface inside the passage. Most of the paper so far has focused on mixing, but effects inside the passage give rise to the mixing process. We discuss the interaction of the secondary flow with the profile suction surface in the following section.

### **The Influence of Secondary Flow Separation From the Profile**

Recall the midwake secondary velocity vectors of Fig. 5 that indicate a spanwise migration of the secondary flow along the profile suction surface. This spanwise flow turns away, or separates from the profile and circulates back towards the endwall. It is suggested that this separation is responsible for generating the expansive low energy regions typical of endwall flows. Energy is lost via viscous dissipation as the separated flow mixes with high-energy fluid.

We investigated the use of profile fences to inhibit the spanwise flow towards midspan on the suction surface, thus isolating the secondary flow from the midspan flow. To the authors' knowledge, Prümper [21] was the first to investigate fences for turbomachinery applications, testing approximately 400 different fence designs. The optimum design consisted of a profile fence and it reduced the area averaged passage loss by 50% for an annular cascade of vanes of aspect ratio unity. We are not advocating the use of fences, but they can elucidate the influence of the secondary flow on energy deficit formation within the passage.

As partially shown in Fig. 9, boundary layer fences were installed on the three center airfoils of the cascade. The center airfoil of the cascade is shown on the left in Fig. 9. Because measurements were obtained in the wake of the center airfoil, its fence was cut to wrap around to the pressure surface to enable attachment without altering the shape of the suction surface. The neighboring airfoil fences, however, were attached to the suction surfaces.

Plumber's putty was applied to the pressure surface of the airfoil adjacent to the center blade suction surface near the endwall. The putty narrowed the passage to reduce the cross-passage pressure gradient and improve the isolating effect of the fence. This application of a thickened or "spooned" profile pressure surface is different than commonly used in practice. Blanco et al. [22] describes how "spooning" the profile is used





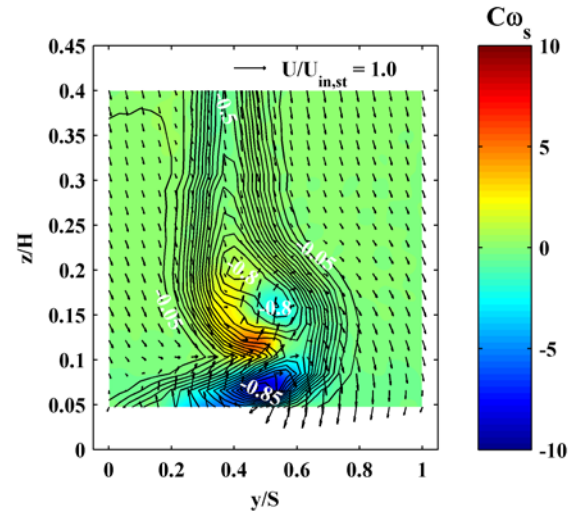
**Figure 9.** Image of cascade airfoils with fence and pressure surface modifications

to reduce the interaction between the pressure surface separation bubble and the endwall flow. Based on the transitional computational model used by Lyall et al. [12] and surface flow visualization, the L2A profile does not have a pressure surface separation bubble at design incidence. The plumber's putty shown in Fig. 9 was applied by hand, so its appearance is not smooth in the picture. Smoothness is not important in creating a reduced cross-passage pressure gradient.

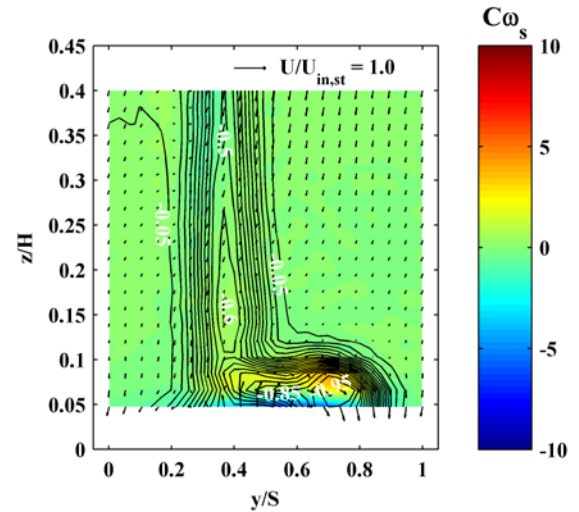
The fences were installed at 4.2% span from the endwall, a distance above the inlet boundary layer thickness. Bloxham's [23] particle image velocimetry measurements on the L1A profile, which has the same gas angles as L2A in the present study, indicated that the spanwise flow of the passage vortex remains close to the suction surface inside the passage. Using Bloxham's [23] measurements as a guide, the sheet metal fences were cut to extend into the flow 8.5% pitch from the suction surface. The leading edges of the fences were at  $0.65C_{ax}$  from the leading edges of the profiles (aft of peak suction).

The effect of the fence and putty on the endwall wake is shown in Fig. 10. One first notes in Fig. 10b that applying the fence and putty caused a nearly two-dimensional flow from  $z/H = 0.12$  on towards midspan. The strong region of positive vorticity in Fig. 10a that has a peak magnitude approximately centered at  $y/S = 0.45$  and  $z/H = 0.12$ , is essentially eliminated using the fences and putty. This positive region of vorticity was eliminated because of the absence of spanwise flow along the profile that would normally skew the boundary layer. Furthermore, because of the absence of the spanwise flow, there is no ability for flow separation to propagate towards midspan. The absence of spanwise flow is why the large low energy region of Fig. 10a that is approximately centered at  $y/S = 0.45$  and  $z/H = 0.18$ , is nearly eliminated using the fences and putty. Without fences and putty, significant endwall effects propagate to approximately 30% span, but to only 12% span with a fence. The secondary velocity vectors also indicate a slight improved average turning in Fig. 10b of approximately less than  $0.5^\circ$ .

The mass-averaged passage loss was reduced by 12.9% using the fences and putty. An experiment using only fences (not shown in Fig. 10), showed that the putty contributed to



**a) No fence or putty**



**b) With fence and putty**

**Figure 10.** Flood plots of secondary vorticity, Y contours, and secondary velocity vectors with and without fences and putty

about 3% of the loss reduction. The authors note that measurements below 4.8% span were not included in the estimate, so the loss reduction may be lower when including measurements all the way to the wall. The purpose of the experiment with the fences and putty, however, was not to develop a loss reduction design, but to bring attention to the importance of the interaction of the secondary flow with the profile suction surface. Inside the passage, the secondary flow vortices climb the profile suction surface and then separate. Losses are generated by mean flow and turbulence dissipation as the separated flow mixes out, forming the low energy cores typical of endwall flows. Mixing continues within and downstream of the blade row.

Past attempts at reducing endwall losses for high lift profiles have generally focused on weakening the vortex structures, such as using non-axisymmetric endwall contouring (e.g., Praisner et al. [2] and Knezevici et al. [3]). Any

modifications to the profile near the endwall that suppress separation of the secondary flow may provide loss reductions additive to those that weaken vortical structures. Such modifications may not be straightforward and need to be researched.

## CONCLUSIONS

In this paper, the origin of cascade mixing losses and the role of secondary flow vortical structures in loss development were investigated. For incompressible and adiabatic cascade flows, losses are generated by mean flow dissipation and turbulence dissipation. Turbulence dissipation, however, is difficult to measure and was not attempted. Keeping in mind that shear stress results in dissipation, an approach was developed to study components of the mixing forces. Among the shear forces that drive mixing and generate loss, turbulent shear was dominant over mean shear, suggesting that turbulence dissipation is the dominant cause of losses.

Due to negligible mean flow shear, the mean flow components of the vortical structures in the secondary flow (e.g., the passage vortex) do not contribute significantly to the mixing loss. Rather, the secondary flow causes the suction surface boundary layer to separate near the endwall. Low energy cores, typical of endwall flows, form inside the passage due to dissipation effects as the separated flow mixes out. An ad hoc experiment using profile boundary layer fences and a pressure surface modification eliminated a large portion of this separation, containing endwall effects to within 12% span. Endwall effects propagated to 30% span without the fences and pressure surface modification. Thus, interaction of the secondary flow with the profile suction surface is very important for loss development.

Modifications that limit the suction surface separation near the endwall can provide loss reductions additive to those that weaken vortical structures, such as endwall contouring. These modifications may not be straightforward and research is needed to investigate the problem.

## REFERENCES

- [1] McQuilling, M.W., 2007. "Design and Validation of a High Lift Low-Pressure Turbine Blade," PhD Thesis, Wright State University, Dayton, Ohio.
- [2] Praisner, T.J., Grover, E.A., Knezevici, D.C., Popovic, I., Sjolander, S.A., Clark, J.P., and Sondergaard, R., 2008, "Toward the Expansion of Low-Pressure-Turbine Airfoil Design Space," ASME Paper GT2008-50898.
- [3] Knezevici, D.C., Sjolander, S.A., Praisner, T.J., Allen-Bradley, E., and Grover, E.A., 2009, "Measurements of Secondary Losses in a High-Lift Front-Loaded Turbine Cascade with the Implementation of Non-Axisymmetric Endwall Contouring," ASME Paper GT2009-59577.
- [4] Moore, J. and Adhye, R.Y., 1985, "Secondary Flows and Losses Downstream of a Turbine Cascade," *J. of Engineering for Gas Turbines and Power*, Vol. 107, pp. 961-968.
- [5] MacIsaac, G.D., Sjolander, S.A., and Praisner, T.J., 2010, "Measurements of Losses and Reynolds Stresses in the Secondary Flow Downstream of a Low-Speed Linear Turbine Cascade," ASME Paper GT2010-22727.
- [6] Gregory-Smith, D.G., Walsh, J.A., Graves, C.P., and Fulton, K.P., 1988, "Turbulence Measurements and Secondary Flows in a Turbine Rotor Cascade," *J. of Turbomachinery*, Vol. 110, pp. 479-485.
- [7] Moore, J., Shaffer, D.M., and Moore, J.G., 1987, "Reynolds Stresses and Dissipation Mechanisms Downstream of a Turbine Cascade," *J. of Turbomachinery*, Vol. 109, pp. 258-267.
- [8] Hinze, J.O., 1975, "Turbulence," 2<sup>nd</sup> Edition. New York, New York: McGraw Hill.
- [9] Panton, R.L., 1996, "Incompressible Flow," 2<sup>nd</sup> Edition. New York, New York: John Wiley & Sons, Inc.
- [10] Pope, S.B., 2000, "Turbulent Flows," 1<sup>st</sup> Edition. Cambridge, UK: Cambridge University Press.
- [11] Narasimha, R., and Prasad, S.N., 1994, "Leading Edge Shape for Flat Plate Boundary Layer Studies," *Experiments in Fluids*, Vol. 17, No. 5, pp. 358-360.
- [12] Lyall, M.E., King, P.I., Sondergaard, R., Clark, J.P., and McQuilling, M.W., 2011, "An Investigation of Reynolds Lapse Rate for Highly Loaded Low Pressure Turbine Airfoils with Forward and Aft Loading," ASME Paper GT2011-46328.
- [13] Lekakis, I.C., Adrian, R.J., and Jones, B.G., 1989, "Measurement of Velocity Vectors with Orthogonal and Non-Orthogonal Triple-Sensor Probes," *Experiments in Fluids*, Vol. 7, pp. 228-240.
- [14] Gieseke, T.J., and Guezennec, Y.G., 1993, "An Experimental Approach to the Calibration and Use of Triple Hot-Wire Probes," *Experiments in Fluids*, Vol. 14, pp. 305-315.
- [15] Kline, S.J., and McClintock, F.A., 1953, "Describing Uncertainties in Single Sample Experiments," *Mechanical Engineering*, Vol. 75.
- [16] Tannehill, J.C., Anderson, D.A., and Pletcher, R.H., 1997, "Computational Fluid Mechanics and Heat Transfer," 2<sup>nd</sup> Edition. Philadelphia, Pennsylvania: Taylor & Francis.
- [17] Moffat, R.J., 1988, "Describing the Uncertainties in Experimental Results," *Experimental and Thermal Fluid Science*, Vol. 1, pp. 3-17.
- [18] Langston, L.S., 2001, "Secondary Flows in Axial Turbines –A Review," *Annals New York Academy of Sciences*, Vol. 934, *Heat Transfer in Gas Turbine Systems*, pp. 11-26.
- [19] Hodson, H.P., and Dominy, R.G., 1987, "Three-Dimensional Flow in a Low-Pressure Turbine Cascade at its Design Condition," *J. of Turbomachinery*, Vol. 109, pp. 177-185.
- [20] Zoric, T., Popovic, I., Sjolander, S.A., Praisner, T., and Grover, E., 2007, "Comparative Investigation of Three Highly Loaded LP Turbine Airfoils: Part I – Measured Profile and Secondary Losses at Design Incidence," ASME Paper GT2007-27537.

- [21]Prümper, H., 1972, "Application of Boundary Layer Fences in Turbomachinery," AGARD-AG-164, pp. 311-331.
- [22]Blanco, E., Hodson, H.P., Vazquez, R., and Torre, D., 2003, "Influence of the State of the Inlet Endwall Boundary Layer on the Interaction between Pressure Surface Separation and Endwall Flows," Proc. Instn Mech. Engrs Vol. 217, Part A: *J. of Power and Energy*, pp. 433-441.
- [23]Bloxham, M.J., 2010, "A Global Approach to Turbomachinery Flow Control: Loss Reduction Using Endwall Suction and Midspan Vortex Generator Jet Blowing," PhD Dissertation, The Ohio State University, Columbus, Ohio.